Magnetic resonance studies of hydration kinetics and microstructural evolution in plaster pastes

K. M. Song · J. Mitchell · L. F. Gladden

Abstract This paper details a comparison of the evolution in the microstructure of the α and β forms of gypsum plaster that occur during hydration. The comparison has been performed using a combination of rapid Nuclear Magnetic Resonance (NMR) relaxation measurements and Scanning Electron Microscopy images, acquired as a function of hydration time. The α plaster hydrates to an interconnected network of uniform gypsum crystals providing a homogeneous structure, whereas the β plaster exhibits growth of crystals with irregular shape leading to a more open pore network and a heterogeneous product. An additional NMR T_2 relaxation time component is observed in the β plaster compared to the α plaster, suggesting the presence of large pores in the β plaster. This conclusion is confirmed by pore volume distributions determined from X-ray micro-computerised tomography (μ-CT) images of the set plasters. To the best of our knowledge, this is the first study of both forms of plaster utilising this combination of experimental techniques. The hydration kinetics have also been compared using one-dimensional NMR profiles, from which effective rate constants are determined. Consistent with previous results, the hydration reactions of the α and β forms of plaster are seen to occur at very different rates: the α plaster has a short initiation period and a slow hydration reaction. In contrast, the β plaster has a long initiation period, although the hydration reaction proceeds more rapidly thereafter. This work demonstrates the applicability of several NMR techniques to monitor, in situ, the hydration kinetics and microstructural evolution in plaster pastes, which will be crucial to the further understanding of mechanical properties (e.g. moisture transport) in these systems.

Introduction

Gypsum ($CaSO_4 \cdot 2H_2O$) is an ancient building material still used today in many industries including the production of fertilizers and as a cement additive, as well as its traditional role as plaster. For modern construction purposes, gypsum is sold commercially in pre-fabricated "plasterboards" for interior wall and ceiling applications. Plasterboards are used widely due to their advantageous mechanical properties of low specific gravity, good thermal and sound insulation, and fire resistance [1]. Manufacture of plasterboard requires energy to remove excess water added to the plaster to provide fluidity. Understanding the evolution of the pore structure during the hydration of the plaster—and hence water transport in the set product—could allow for the development of more energy efficient drying processes, and lead to improved quality of the plasterboard.

In the manufacture of plaster, gypsum is first partially dehydrated to produce calcium sulfate hemihydrate ($CaSO_4 \cdot 0.5H_2O$) powder, referred to commonly as "Plaster of Paris". The plaster powder is manufactured by either a "wet" (autoclaved) or "dry" (calcined) industrial process, and is categorised subsequently as α or β plaster, respectively [2]. Both forms are used in commercial plaster products. When the dried plaster powder is mixed with water, the resulting paste hardens as the water combines with the hemihydrate to produce crystalline gypsum dihydrate. This change in microstructure during hydration results in a high porosity material whose mechanical properties depend on the pore structure.

K. M. Song · J. Mitchell (✉) · L. F. Gladden
Department of Chemical Engineering and Biotechnology,
University of Cambridge, Pembroke Street,
Cambridge CB2 3RA, UK
e-mail: jm600@cam.ac.uk

The hydration of plaster to crystalline gypsum has been the subject of many investigations, and a vast amount of data is distributed throughout the literature; a review of this subject has been presented by Singh and Middendorf [3]. Here we identify earlier reports that have used different methods to compare the α and β forms. Early optical microscopy images revealed differences in the macroscopic structure of individual α and β crystals during dehydration [4, 5]. Using infrared spectroscopy, X-ray diffraction, and Differential Thermal Analysis (DTA), Bensted and Varma [6] suggested, in agreement with earlier works [2, 7], that the only difference between the two forms is particle size. However, there is evidence from more recent X-ray powder diffraction and solid-state ^{1}H NMR that suggest differences in crystal structure do exist between the two forms [8] and these differences can be related to the reactivity of the hemihydrates with water and the mechanical strength of the dihydrate products [5].

The kinetics of hydration for both the α and β forms of plaster have been monitored previously using thermal analysis and electrical resistance [9, 10], strength and acoustic transmission [11], and luminescence rigidochromism [12]. The β plaster was observed consistently to exhibit a longer initiation period (delay preceding the hydration) than the α plaster, yet the hydration reaction occurred more rapidly in the β form.

Techniques used to characterise the microstructure of porous materials include Mercury Intrusion Porosimetry (MIP) [13], N_2 gas adsorption [14], Differential Scanning Calorimetry (DSC) thermoporometry [15], Small Angle Neutron Scattering (SANS) [16], and Nuclear Magnetic Resonance (NMR) cryoporometry [17, 18]. The microstructure of α and β gypsum products has been studied previously using scanning electron microscopy (SEM) [3, 11, 19], where the α dihydrate was seen to be composed of regular, interlocking crystals whilst the β dihydrate contained smaller, irregular crystals. All of the characterisation techniques listed above require the hydration process to be interrupted, perturbing the evolution of the microstructure. They are considered reliable for materials with static pore structures but less suitable for the study of hydrating plaster that evolves continuously. In contrast, NMR relaxometry can probe directly the water in the plaster paste and the results used to infer structural changes. If the NMR data are acquired on a time scale short compared to the hydration time, then the kinetics and microstructure evolution that occurs during hydration can be probed non-destructively and in situ without interrupting the reaction.

The NMR relaxation rate constants $1/T_1$ and $1/T_2$ of a liquid imbibed in a porous media are proportional to the surface-to-volume ratio S/V of the pore structure [20, 21]. These relaxation times (T_1 and T_2) have been used for

several years to study the microstructure of hydrating cement pastes: a small selection of the literature is represented in the references given here [22–29]. Two-dimensional relaxation correlations have also been used to further elucidate the pore structures in cement pastes [30, 31]. A wider range of techniques can be applied more easily to cements since the hydration time is considerably longer than for plaster, where complete hydration can occur in less than one hour. Previously, T_2 relaxation time measurements have been used to monitor the evolving pore structures in plaster paste because the data acquisition time is short compared to the overall hydration time. Jaffel et al. [32] observed two distinct water populations in β plaster paste, and the variations in the relative water fraction of these populations were monitored as a function of hydration time for a range of water-to-plaster ratios w/p. The pore structures determined from the NMR data were supported by SEM images of the set products, and were related to the macroscopic mechanical properties of the plaster via ultrasound velocity measurements [33]. The macroscopic and microscopic transport of water in fully hydrated plaster pastes was also investigated with T_2 relaxation analysis [32]. Elsewhere it has been shown that the hydration of plaster can be followed using T_2 relaxation measurements on a low-field, portable NMR device [34].

In this article, we extend the work of Jaffel et al. by comparing the kinetics and microstructural evolution during the hydration of the α and β forms of plaster. The hydration kinetics are determined using a basic one-dimensional spin-echo imaging sequence [35] that is sensitive only to the mobile water in the pore voids and not to the bound water in the gypsum crystals, because the T_2 relaxation time of the bound water is too fast to be detected with this imaging technique. As the hydration occurs, the signal intensity in the profile decreases, and so a reaction rate can be inferred. Here, both T_2 and T_1 relaxation times are obtained on a time scale short compared to the hydration time of the plaster. This has been achieved using single-shot Carr–Purcell–Meiboom–Gill (CPMG) [36, 37] echo trains and a rapid double-shot T_1 measurement [38, 39], respectively. At high magnetic field strengths ($\mathbf{B}_0 > 1$ T, as used here) the T_2 measurement is affected by magnetic field gradients caused by susceptibility differences in the sample. As a result, the longitudinal T_1 relaxation time is considered to be a more direct probe of pore surfaces since it is unaffected by the internal gradients [40]. However, conventional T_1 NMR measurements such as inversion or saturation recovery [41] have been considered too slow to provide both good time resolution and high quality data during 1 h of hydration. The rapid T_1 measurement implemented here has been shown elsewhere to provide accurate, quantitative relaxation times [42]. We also monitor the microstructural evolution using SEM

images acquired at various times during the hydration process. Whilst other authors have presented SEM images of gypsum-based materials during hydration [11, 43] we have presented a coherent set of SEM images comparing the microstructural changes in the α and β forms of plaster during hydration. The final, set plasters have been imaged using SEM and X-ray micro-computerised tomography (μ-CT), used previously to study the structure of hydrating cement pastes [44], to confirm the differences in pore structure implied by the NMR relaxation measurements. We use this combination of experiments to compare the hydration kinetics and microstructure in the α and β forms of plaster.

Materials and methods

Commercial α and β gypsum plaster powders with a purity of >98 wt% were used in all the experiments. The samples were prepared by manual mixing of the plaster powder with deionised water at a $w/p = 0.8$ by weight to form a paste (slurry).

For the NMR studies, approximately 50 g of the plaster pastes were poured into 25×100 mm^2 (diameter $\times$ height) glass tubes and sealed to limit evaporation during the hydration time. The NMR experiments were performed using a Bruker AV spectrometer connected to a 2 T horizontal bore imaging magnet (85 MHz for ^{1}H). The glass tubes were positioned horizontally in the birdcage radio frequency (r.f.) coil. Excitation pulse lengths of $t_{90} = 15$ μs and $t_{180} = 30$ μs corresponding to tip angles of 90° and 180° were typical. For the hydration kinetics studies, a standard one-dimensional spin-echo imaging sequence was employed to obtain profiles of 128 pixels along the length of the samples at a resolution of $\Delta z \sim 1.56$ mm per pixel. The echo time was $\tau = 2$ mm and each profile was acquired in 25 s. For the microstructural analysis, CPMG echo trains were acquired with 1024 echoes, separated by $2\tau = 800$ μs. Each CPMG decay, with 2 scans, was acquired in 1 min. In the double-shot T_1 measurements, 32 data points were acquired, separated uniformly by 5 ms. Each data set, with 8 scans, was acquired in less than 2 min. In each case, the NMR data were acquired at 3-min intervals throughout the 50-min hydration period. Although T_1 measurements can be acquired on a similar time scale using conventional saturation recovery [41], the double-shot T_1 technique provides more data points and improved signal-to-noise ratio S/N (due to an increase in the number of repeat scans) for the same total experimental time compared to saturation recovery. Also, the exponential decay provided by the double-shot T_1 sequence can be fitted unambiguously because the fit function does not require an accurate measure of the total magnetisation,

unlike the exponential growth obtained from the saturation recovery sequence.

For the SEM imaging, samples of plaster paste were soaked in 2-propanol to stop the hydration at different stages before being dried overnight at 45 °C. The SEM images of the gypsum crystals were acquired with a LEO 1530 and Supra VP Gemini scanning electron microscope utilising a field-emission gun at an acceleration voltage of 3 kV.

For the μ-CT imaging, wet plaster pastes were introduced into 1.6×10 mm^2 sample tubes, allowed to hydrate for 60 min (corresponding to complete hydration [10]), and then dried overnight. The μ-CT images were obtained using a SkyScan 1072 μ-CT scanner with a tungsten anode operating at 46 kV and 219 μA. The samples were then analysed using a 0.5 mm Al filter. The total rotation angle of the sample was 180°, with a rotation step angle of 0.45°, allowing 400 two-dimensional images to be acquired. These were reconstructed into three-dimensional images of the samples with a resolution of $3.11 \times 3.11 \times 3.11$ μm^3 per voxel.

Results and discussion

Hydration kinetics

The hydration kinetics of both α and β plasters were determined from one-dimensional NMR profiles. The echo time in the profile acquisition of $\tau = 2$ ms meant that the bound water, with $T_2 \approx 10$–20 μs, could not be detected and only the mobile water in the pore voids was observed. The time series of profiles, acquired during in situ hydration are shown in Fig. 1 for the (a) α and (b) β forms of plaster, respectively. The irregular shape of the profiles is a result of water rising to the top of the sample tube when the paste was introduced initially. The signal intensity is seen to decrease in both plasters during hydration as a fraction of the mobile water becomes bound in the gypsum crystals. In the α plaster the signal intensity is seen to decrease at a constant rate with time, indicated by the uniform spacing between the profiles. In contrast, the β plaster hydrates at a non-uniform rate. The initial profiles (corresponding to a hydration time ≤15 min) have a constant intensity, indicative of a long initiation period, after which the hydration occurs rapidly.

To examine the hydration kinetics in more detail, the signal intensity was averaged across the top of each profile (30–70 mm) in Fig. 1. These average signal intensities can be seen as a function of hydration time in Fig. 2. Three different stages of hydration are visible, corresponding to the initiation period, the acceleration period, and the completion period. The initiation period is observed as a
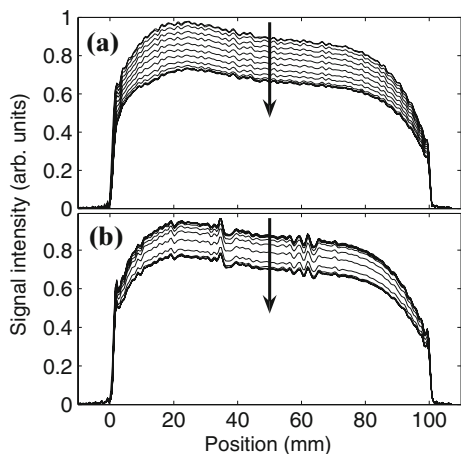
Fig. 1 NMR profiles acquired during the hydration of **a** α and **b** β plaster at $w/p = 0.8$. The profiles were acquired at regular intervals of 3 min. Increasing hydration time is indicated by the *arrow* in each case, with the profiles acquired between 2 (*top profile*) min and 42 (*bottom profile*) min of hydration. The irregular profile shape is a result of the sample preparation (see text for details); the top of the sample as prepared is at 0 mm
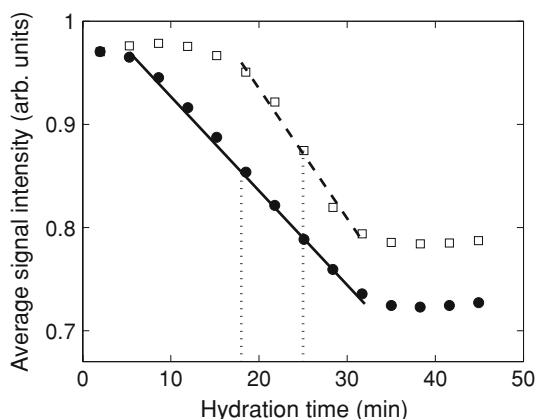
Fig. 2 Comparison of hydration dynamics for α (*filled circle*) and β (*open square*) plasters at $w/p = 0.8$. Reaction rates of $k_\alpha = 0.009 \pm 0.003 \text{ s}^{-1}$ and $k_\beta = 0.015 \pm 0.005 \text{ s}^{-1}$ were determined by fitting straight lines to the acceleration periods of the α (*solid line*) and β (*dashed line*) plasters, respectively. The characteristic activation times (*dotted lines*) are 18 and 25 min for the α and β plasters, respectively

plateau in the signal intensity: this is pronounced in the β plaster, where the initiation period extends to ∼18 min of hydration time. The α plaster exhibits a very short initiation period (<5 min).

The acceleration period encompasses the actual gypsum crystallisation, and is observed as a decrease in the profile signal intensity as a function of hydration time in Fig. 2. By fitting a straight line to the data points corresponding to the acceleration period, approximate reaction rates of $k_\alpha = 0.009 \pm 0.003 \text{ s}^{-1}$ and $k_\beta = 0.015 \pm 0.005 \text{ s}^{-1}$ were determined for the α and β plasters, respectively. Although these

rates are only semi-quantitative due mainly to the variable T_2 relaxation contrast in the profiles, they indicate clearly that the hydration reaction proceeds much more rapidly in the β plaster compared to the α plaster, in agreement with other authors [9, 10, 12]. It is also possible to define an activation time from the average crystallisation time (i.e. the mid-point of the acceleration period). Activation times of 18 and 25 min were determined for the α and β plasters, respectively, and these times are indicated in Fig. 2 (dotted lines).

Once the gypsum crystallisation process had finished, the signal intensity remained constant; this is the completion period. Despite the significant difference in the reaction rates, both plasters required the same time to hydrate completely. This is due to the long initiation period of the β plaster. The final average signal intensities in Fig. 2 are different for the two plasters: for the α plaster the average signal intensity after hydration is 0.72, and for the β plaster, 0.78. The stoichiometric fraction of water required for hydration is 0.23 for both plasters, so the amount of water consumed in the hydration reaction should be similar, as is observed. The small difference observed may result from the α plaster containing impurities that consume additional water on hydration. However, it is far more likely that the relaxation weighting on the profiles in Fig. 1, which will be sensitive to porosity, accounts for this difference.

Many authors have hypothesised as to the underlying variations governing the different reaction rates. For example, a higher surface area in the β plaster providing more nucleation sites for the crystallisation of gypsum could increase the hydration rate [3]. Conversely, the α plaster powder, which has been shown to have a crystal habit with more preferential sites for the chemical adsorption of water, could exhibit a faster dissolution rate reducing the initiation period [10]. Elsewhere, differences in the hydration dynamics have been attributed to varying particle size distributions or impurities in the raw materials [45]. Whilst the hydration reaction rates presented here provide no indication as to the underlying control mechanism, the simplicity and clarity of the method and results will allow these hypotheses to be examined rigorously in future work.

Pore structure evolution

The transverse relaxation rates determined for the water contained within the plaster paste during hydration provide direct information on the evolution of the pore structure. In the fast exchange limit, $1/T_2 \propto S/V$ [20, 21], and hence $T_2 \propto \langle x \rangle$ where $\langle x \rangle$ is a characteristic mean pore size. The precise scaling depends on the surface relaxivity constant ρ, such that $1/T_2 \approx \rho \, S/V$, and this has been shown

elsewhere to vary within similar materials [46], making a conversion from relaxation time to pore size difficult to calibrate [31]. The density of surface paramagnetic impurities in the plaster powders could be different, and so it is unwise to compare the measured relaxation times of the α and β plasters directly. However, orders of magnitude and trends can be used to infer the scales of pores (large or small) and the microstructural evolution. The CPMG decays determined for liquids imbibed in inhomogeneous porous media tend to be complex exponential functions, so it is usual to convert the data into distributions of relaxation times using a numerical inverse referred to popularly as a Laplace transform. This is an inherently ill-posed problem and requires some constraints to produce a stable solution. Here we use Tikhonov regularisation [47, 48] with the regularisation (smoothing) parameter determined by the Generalised Cross Validation (GCV) method [49, 50]. Figure 3 shows a selection of the regularised T_2 relaxation time distributions determined during the hydration of the α and β plasters.

Both of the plasters exhibit two distinct peaks in the initial T_2 relaxation time distributions. A dominant peak at long T_2 times corresponds to water in large pores or bulk, and a significantly smaller peak at short relaxation times corresponds to water in the fine pore structures. For the α plaster, Fig. 3a, the peaks are initially centred on $T_2 = 8$ and 45 ms. As the hydration proceeds and the pore structure evolves, these peaks shift to shorter relaxation times. When the hydration has concluded (after 47 min), the peaks are centred on $T_2 = 5$ and 25 ms. This indicates that the average pore size in each population is decreasing, although the simultaneous broadening of the two peaks
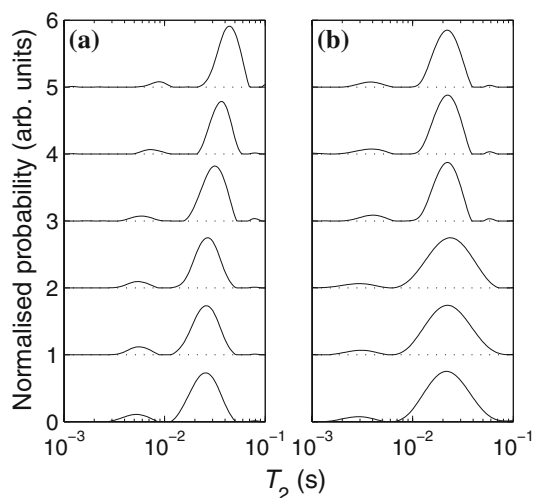
suggests that the pore structure is becoming more inhomogeneous as the pores develop.

For the β plaster, Fig. 3b, the peaks are centred on $T_2 = 4$ and 22 ms initially. As the hydration reaction progresses, the short relaxation time peak shifts to $T_2 = 3$ ms yet remains relatively consistent in width. The long relaxation time peak broadens considerably whilst staying centred at $T_2 = 22$ ms throughout the hydration time. This suggests that the hydration leads, predominantly, to the development of a heterogeneous distribution of large pores.

To further clarify the relaxation time behaviour during hydration, and to remove some of the uncertainty inherent in the numerical inversion, the CPMG decays were fitted using discrete two- or three-component exponential functions as appropriate, selected by examining the residual χ^2 fit errors. The relaxation times determined by this method are shown in Fig. 4 for the (a) α and (b) β plasters, respectively. As observed in the T_2 relaxation time distributions, Fig. 3, two distinct relaxation time components are observed initially for each form of plaster.

In the case of the α plaster, Fig. 4a, the two relaxation times are seen to decrease from $T_2 = 12$ and 45 ms throughout the acceleration period of the hydration process, corresponding to a hydration time <35 min, as the pore structure evolves. The final relaxation times—static throughout the completion period—are $T_2 = 8$ and 28 ms. These values correspond well with the peaks centred at $T_2 = 5$ and 25 ms seen in the relaxation time distributions.

Two T_2 relaxation time components are observed initially in the β plaster, Fig. 4b, corresponding to $T_2 = 8$ and 24 ms. These values remained constant throughout the initiation period (hydration time <18 min). At the start of

Fig. 3 T_2 relaxation time distributions for a α and b β plasters at $w/p = 0.8$, measured at hydration times of (top to bottom) 2, 11, 20, 29, 38, and 47 min. The area under the distributions has been normalised relative to the initial signal intensity for each sample
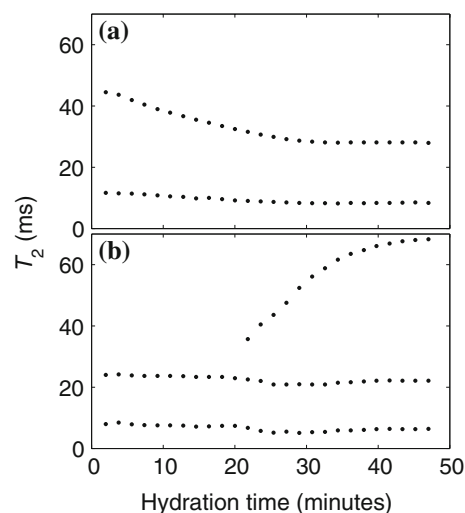
Fig. 4 Variation of T_2 relaxation times during the hydration of a α and b β plasters at $w/p = 0.8$ determined by fitting two- or three-component exponential decays to the CPMG data as appropriate

the acceleration period, when the hydration reaction proceeds (hydration time 18–20 min), the data become well-fitted only by a three-component exponential decay. An apparent decrease in the two short relaxation time components is observed around 20–28 min hydration time. Although this slight decrease ($T_2 = 24$–22 ms for the long component; $T_2 = 8$–6 ms for the short component) may be a genuine reflection of a reduction in the pore size during the hydration process, we cannot exclude the possibility that it is an artefact introduced by the shift from a two-component to a three-component fit. The significant feature of Fig. 4b is the increase in the long (third) T_2 relaxation time component from $T_2 = 36$–68 ms during the acceleration period. This clearly indicates that large pore voids are opening up in the gypsum structure and is consistent with the broadening of the long relaxation time component peak observed in the T_2 distributions. During the completion period (hydration time >42 min) the short relaxation time components remain constant. The long relaxation time component appears to be still increasing during the completion period, although given the experimental and fit errors on the data, this is not conclusive evidence for continued evolution of the large pores.

It should be noted here that the significant difference in the final T_2 relaxation times observed will account for some of the difference in the signal intensity of the profiles seen in Fig. 1. The short T_2 relaxation times of the water in the α plaster cause enhanced signal attenuation during the acquisition of the spin-echo profiles, whereas the long, dominant T_2 relaxation component in the β plaster will provide less attenuation. This supports our conclusion in section Hydration kinetics that the difference in the final average signal intensities in Fig. 2 originates from the effects of relaxation contrast.

The plots of discrete, average, relaxation time components (Fig. 4) are considerably more useful for highlighting the trends in pore network development than the relaxation time distributions (Fig. 3). Using the rapid double-shot T_1 measurement, we have also monitored the T_1 behaviour as a function of hydration time in both plaster pastes. The results are shown in Fig. 5. Here, in contrast to the multi-component T_2 decays, the T_1 data were well-fitted by a single component exponential function. This can be explained by the fact that the T_1 measurement probes the water/pore surface interactions on a different time scale to the T_2 measurement. The T_2 measurement can be considered as a local probe of the pore surface. However, during the longer observation times in the T_1 measurements, mobile water molecules can explore more of the pore network, and so T_1 provides an indicator for S/V averaged over a greater length scale. In the α plaster, Fig. 5a, the T_1 relaxation time decreases from $T_1 = 1.22$–0.77 s across the acceleration period, suggesting the formation of a solid
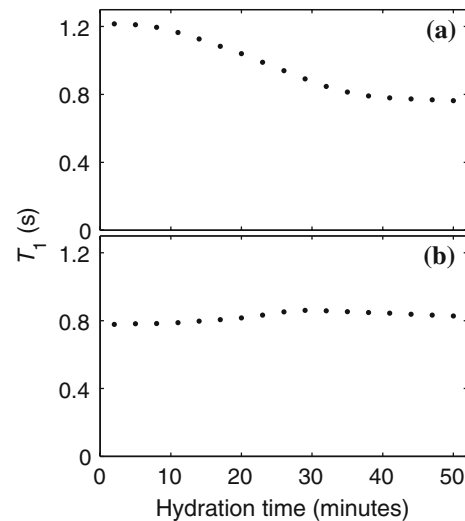
Fig. 5 Variation of T_1 relaxation times during the hydration of **a** α and **b** β plasters at $w/p = 0.8$ determined by fitting a single component exponential decay to the double-shot T_1 data

matrix with small pores. In the β plaster, Fig. 5b, the average T_1 does not vary greatly during the hydration; a slight increase from $T_1 = 0.77$–0.86 s occurs across the acceleration period (hydration time 20–30 min) indicating an increase in the average pore size. This is followed by a slight decrease to $T_1 = 0.83$ s that cannot be easily explained, although it may simply represent a gradual redistribution of the water in the pore network.

Morphology of hydrated plaster

To confirm the variations in pore structure implied by the NMR results, the crystal structures in the hydrating plasters were examined by SEM. Figure 6 shows the crystal structure in the α plaster at various times during the
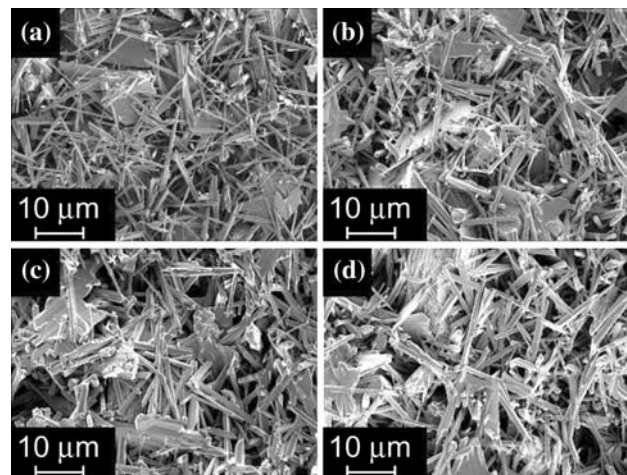
Fig. 6 SEM images of α plaster at $w/p = 0.8$ after **a** 11, **b** 20, **c** 29, and **d** 38 min of hydration. Images acquired at ×5000 magnification

Fig. 7 SEM images of β plaster at $w/p = 0.8$ after **a** 11, **b** 20, **c** 29, and **d** 38 min of hydration. Images acquired at $\times5000$ magnification
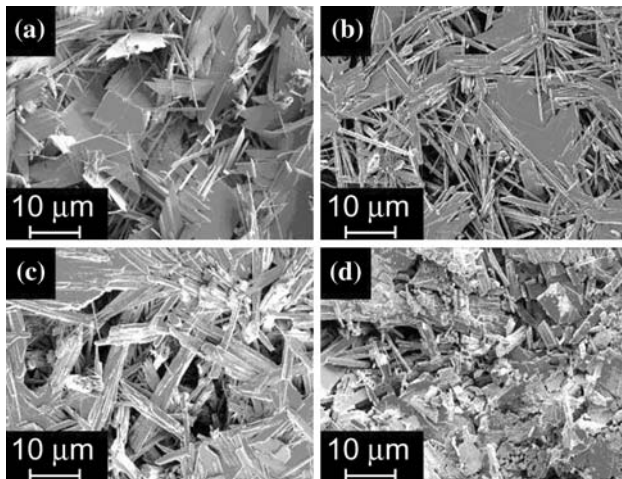
Fig. 8 SEM images of **a** α and **b** β plaster at $w/p = 0.8$ after 50 min of hydration. Images acquired at $\times20000$ magnification

hydration. At a hydration time of 11 min, Fig. 6a, the gypsum crystals have already nucleated and formed thin, needle-like structures. As the gypsum continues to hydrate, Fig. 6b–d, the crystals grow in length and thickness. These developing crystals become entangled to form a high porosity material. The pores evolve as the crystal entanglement and interaction continues throughout the acceleration period of hydration. Overall, a gradual change in the physical structure during the hydration of the α plaster is observed, in agreement with the T_1 and T_2 measurements.

Figure 7 shows the morphology of the β plaster gypsum crystals at various stages during the hydration. During the initiation period (11 min; Fig. 7a) large, plate-like structures are observed. At the start of the acceleration period (20 min; Fig. 7b), small, needle-like crystals can be seen, akin to those observed in the α plaster. However, as the hydration progresses in the β plaster, these thin crystals broaden rapidly and become irregular in shape. At the end of the acceleration period (38 min, Fig. 7d), short, thick crystals with relatively little inter-crystalline entanglement (compared to the α plaster) are visible.

The salient difference between the gypsum crystal structures in the hydrated α and β plasters is highlighted in Fig. 8. At higher magnification, the α crystals, Fig. 8a, appear to be regular in shape and interwoven. In contrast, the β crystals, Fig. 8b, are thicker, shorter, and appear to be stacked rather than entangled. Some crystals also seem to exhibit fractures and there is a quantity of "grainy" material. The SEM images in Fig. 8 are in agreement with SEM images of hydrated gypsum products published previously [3, 11, 19]. The significant difference in the crystal habits of the two plasters is due to the different hydration mechanisms [11]. The rapid hydration reaction in the β plaster clearly results in more heterogeneous pore spaces,
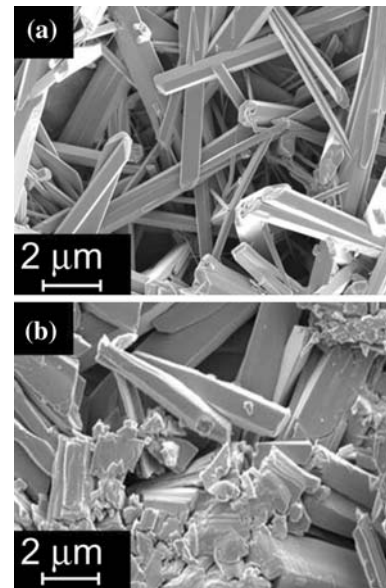
as noted from the NMR relaxation measurements, and less well-defined crystals, as seen in the SEM images.

The macroscopic variation in microstructure between the hydrated plasters can be seen from the μ-CT images in Fig. 9a and b for the α and β forms, respectively. The α
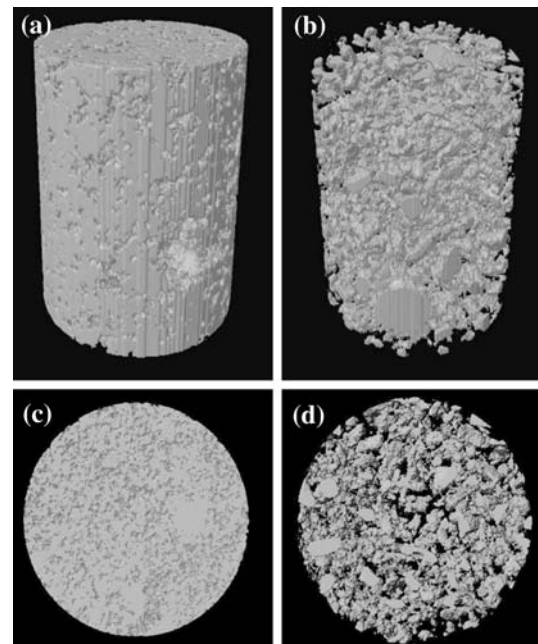
Fig. 9 Three-dimensional structures rendered from μ-CT images of **a** α and **b** β plaster at $w/p = 0.8$ after 60 min of hydration. Each image is a 3×1.6 mm^2 (length $\times$ diameter) section acquired in the middle of each sample, and each voxel is $3.11 \times 3.11 \times 3.11$ μm^3. Two-dimensional cross-sections of the **c** α and **d** β plaster extracted from **a** and **b**, respectively

plaster is a uniform, homogeneous material with a fine pore structure. Only a few larger pores (or cracks) are visible in the surface of the rendered volume. In contrast, the β plaster forms an apparently friable, heterogeneous structure dominated by large pore voids. The details of the porosity are visualised more clearly in the cross-sectional images, Fig. 9c and d, for the α and β plasters respectively. These images were extracted from the three-dimensional, rendered structures.

From the μ-CT images, it is possible to determine pore volume distributions by applying a binary gate to the images as explained elsewhere [51]. The distributions extracted from the images in Fig. 9 are shown in Fig. 10 for the set α and β plasters. The α plaster has a pore radius distribution ranging from $R = 0$–65 μm with a mean pore radius of $R \approx 30$ μm. The β plaster exhibits a broader distribution, ranging from $R = 0$–75 μm, with a mean pore radius of $R \approx 40$ μm. The mean and variance of these distributions agree with the T_2 distributions in Fig. 3, where the β plaster was observed to exhibit a larger mean and variance in T_2 compared to the α plaster. There is also evidence for a population of large pores, $R \approx 70$ μm, in the pore volume distributions of the β plaster, and this supports the presence of a long T_2 component (corresponding to large pores) observed exclusively in the β plaster in Fig. 4. In summary, the μ-CT images confirm the differences in pore structure deduced from the NMR relaxation data. It is interesting to note that the variation in T_2 relaxation time seen in Fig. 4 follows the physical changes in pore structure more closely than the T_1 data. Conventionally, T_1 is considered a more direct measure of S/V, and hence pore size, because it is not influenced by internal, susceptibility induced magnetic field gradients.
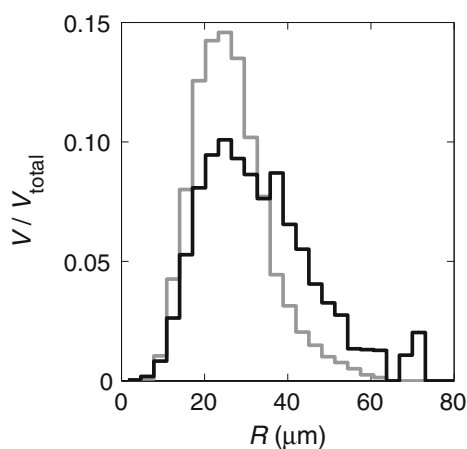
This is true for the results determined for the α plaster where the T_1 relaxation times revealed the reduction in mean pore size during hydration. However, in the case of the β plaster it is clear from the μ-CT images that a homogeneous pore network does not exist. It is therefore reasonable to conclude that, under such conditions, the assumption of $1/T_1 \propto S/V$ is no longer valid. The T_2 measurement continues to probe the local surface interactions, and hence can provide information on the evolution of the plaster even in this heterogeneous system.

Conclusion

A variety of techniques have been used in combination to compare the kinetics and evolution of microstructure during the hydration of the α and β forms of gypsum-based plasters. One-dimensional NMR profiles were used to determine the reaction kinetics during in situ hydration. The β plaster was seen to hydrate significantly faster than the α plaster, although it exhibited a long initiation period, in agreement with previous works. Rapid NMR relaxation measurements of T_1 and T_2 allowed the development of porosity to be monitored during hydration. The α plaster appeared to have fine pore structures and the average pore size decreased during hydration as the gypsum crystals developed. The β plaster was dominated by large pores that increased in size during hydration. These results were confirmed by SEM images recorded at various stages throughout the hydration process: the α gypsum crystals were regular in shape and interwoven. By comparison, the β gypsum crystals were thicker, fractured, and less entangled. SEM of the final, set products were consistent with those published previously. μ-CT images of the set plasters revealed that these microstructural differences were conveyed to the macroscale where the α plaster was homogeneous and the β plaster was seen to be inhomogeneous with large voids of highly irregular shape.

From the results presented here, it is possible to conclude that the rapid hydration and open pore structure of the β plaster would be advantageous in the manufacture of plasterboard, assuming the long induction period can be reduced by further disintegration of the dry powder. The large pore voids increase the efficiency of water transport, and should reduce the drying time required, as long as the mechanical integrity of the product is not impaired. In future work we will continue to explore the evolution of pore structure and water transport using rapid two-dimensional NMR relaxation correlations and NMR diffusion measurements to investigate the influence of initial particle size of the hemihydrate on induction time, and attempt to correlate the microstructure with macroscopic mechanical properties of the hydrated plasters.

Fig. 10 Pore volume distributions (V/V_{total}) as a function of pore radius (R) for the α (grey line) and β (black line) plaster at a $w/p = 0.8$ after 60 min hydration, determined from the μ-CT images in Fig. 9

References

1. Karni J, Karni E (1995) Mater Struct 28:92
2. Goto M, Molony B, Ridge MJ, West GW (1966) Aust J Chem 19:313
3. Singh NB, Middendorf B (2007) Prog Cryst Growth Charact Mater 53:57
4. Miyazaki H (1968) Shinku Kagaku 15:113
5. Šatava V (1970) Sprechsaal Keramik Glas Email 103:792
6. Bensted J, Varma SP (1972) Cem Technol 3:67
7. Ridge MJ, Beretka J (1969) Rev Pure Appl Chem 19:17
8. Follner S, Wolter A, Preusser A, Indris S, Silber C, Follner H (2002) Cryst Res Technol 37:1075
9. Ludwig U, Singh NB (1978) Cem Concr Res 8:291
10. Lewry AJ, Williamson J (1994) J Mater Sci 29:5279. doi: 10.1007/BF01171536
11. Lewry AJ, Williamson J (1994) J Mater Sci 29:5524. doi: 10.1007/BF00349943
12. Kunkely H, Vogler A (2008) Mater Chem Phys 109:506
13. Ritter H, Drake L (1945) Ind Eng Chem 17:782
14. Brunauer S, Emmett P, Teller E (1938) J Am Chem Soc 60:309
15. Brun M, Lallemand A, Quinson JF, Eyraud C (1977) Thermochim Acta 21:59
16. Feigin L, Svergun D (1987) Structure analysis by small-angle X-ray and neutron scattering. Plenum Press, New York
17. Strange JH, Rahman M, Smith EG (1993) Phys Rev Lett 71:3589
18. Mitchell J, Webber JBW, Strange JH (2008) Phys Rep 461:1
19. Kuzel HJ, Hauner M (1987) Zement-Kalk-Gips 40:628
20. Brownstein KR, Tarr CE (1979) Phys Rev A 19:2446
21. Gallegos DP, Munn K, Smith DM, Stermer DL (1987) J Colloid Interf Sci 119:127
22. Bhattacharja S, Moukwa M, Dorazio F, Jehng JY, Halperin WP (1993) J Adv Cem Based Mater 1:67
23. Halperin WP, Jehng JY, Song YQ (1994) Magn Reson Imaging 12:169
24. Mendelson KS, Halperin WP, Jehng JY, Song YQ (1994) Magn Reson Imaging 12:207
25. Jehng JY, Sprague DT, Halperin WP (1996) Magn Reson Imaging 14:785
26. Barberon F, Korb JP, Petit D, Morin V, Bermejo E (2003) Phys Rev Lett 90:116103
27. Nestle N (2004) Cem Concr Res 34:447
28. Plassais A, Pomies MP, Lequeux N, Korb JP, Petit D, Barberon F, Bresson B (2005) Phys Rev E 72:041401
29. Korb JP, Monteilhet L, McDonald PJ, Mitchell J (2007) Cem Concr Res 37:295
30. McDonald PJ, Korb JP, Mitchell J, Monteilhet L (2005) Phys Rev E 72:011409
31. Monteilhet L, Korb JP, Mitchell J, McDonald PJ (2006) Phys Rev E 74:061404
32. Jaffel H, Korb JP, Ndobo-Epoy JP, Morin V, Guicquero JP (2006) J Phys Chem B 110:7385
33. Jaffel H, Korb JP, Ndobo-Epoy JP, Guicquero JP, Morin V (2006) J Phys Chem B 110:18401
34. Boguszynska J, Brown MCA, McDonald PJ, Mitchell J, Mulheron M, Tritt-Goc J, Verganelakis DA (2005) Cem Concr Res 35:2033
35. Callaghan PT (1991) Principles of nuclear magnetic resonance microscopy. Clarendon, Oxford
36. Carr H, Purcell E (1954) Phys Rev 94:630
37. Meiboom S, Gill D (1958) Rev Sci Instrum 29:668
38. Hsu JJ, Lowe IJ (2004) J Magn Reson 169:270
39. Sigmund EE, Caudal N, Song YQ (2006) Solid State Nucl Magn Reson 29:232
40. Washburn KE, Eccles CD, Callaghan PT (2008) J Magn Reson 194:33
41. Vold R, Waugh J, Klein M, Phelps D (1968) J Chem Phys 48:3831
42. Chandrasekera TC, Mitchell J, Fordham EJ, Gladden LF, Johns ML (2008) J Magn Reson 194:156
43. Winkler M, Monaghan P, Gilbert JL, Lautenschlager EP (1995) Dent Mater 11:226
44. Gallucci E, Scrivener K, Groso A, Stampanoni M, Margaritondo G (2007) Cem Concr Res 37:360
45. Kuzel HJ (1987) Neues Jb Miner Abh 156:155
46. Mitchell J, Stark SC, Strange JH (2005) J Phys D Appl Phys 38:1950
47. Munn K, Smith DM (1986) J Colloid Interf Sci 119:117
48. Wilson JD (1992) J Mater Sci 27:3911. doi:10.1007/BF00545476
49. Wahba G (1977) SIAM J Numer Anal 14:651
50. Wahba G (1982) Constrained regularization for ill-posed linear operator equations, with applications in meteorology and medicine. In: Gupta SS, Berger JO (eds) Statistical theory and related topics III, vol 2. Academic Press, New York, pp 383–418
51. Sederman AJ, Alexander P, Gladden LF (2001) Powder Technol 117:255